

## ARTICLE OPEN



# Ocean-forcing of cool season precipitation drives ongoing and future decadal drought in southwestern North America

Richard Seager <sup>1</sup>, Mingfang Ting <sup>2</sup>, Patrick Alexander<sup>1</sup>, Haibo Liu <sup>1</sup>, Jennifer Nakamura <sup>1</sup>, Cuihua Li<sup>1</sup> and Matthew Newman <sup>3</sup>

The US Southwest is in a drought crisis that has been developing over the past two decades, contributing to marked increases in burned forest areas and unprecedented efforts to reduce water consumption. Climate change has contributed to this ongoing decadal drought via warming that has increased evaporative demand and reduced snowpack and streamflows. However, on the supply side, precipitation has been low during the 21st century. Here, using simulations with an atmosphere model forced by imposed sea surface temperatures, we show that the 21st century shift to cooler tropical Pacific sea surface temperatures forced a decline in cool season precipitation that in turn drove a decline in spring to summer soil moisture in the southwest. We then project the near-term future out to 2040, accounting for plausible and realistic natural decadal variability of the Pacific and Atlantic Oceans and radiatively-forced change. The future evolution of decadal variability in the Pacific and Atlantic will strongly influence how wet or dry the southwest is in coming decades as a result of the influence on cool season precipitation. The worst-case scenario involves a continued cold state of the tropical Pacific and the development of a warm state of the Atlantic while the best case scenario would be a transition to a warm state of the tropical Pacific and the development of a cold state of the Atlantic. Radiatively-forced cool season precipitation reduction is strongest if future forced SST change continues the observed pattern of no warming in the equatorial Pacific cold tongue. Although this is a weaker influence on summer soil moisture than natural decadal variability, no combination of natural decadal variability and forced change ensures a return to winter precipitation or summer soil moisture levels as high as those in the final two decades of the 20th century.

*npj Climate and Atmospheric Science* (2023)6:141; <https://doi.org/10.1038/s41612-023-00461-9>

## INTRODUCTION

Drought is no stranger to the southwest of the United States. The region has undergone dramatic fluctuations in aridity during the instrumental period and over the last millennium<sup>1–4</sup>. However, the regional population grew more rapidly than the US as a whole for every decade of the post World War II era (see <https://www.census.gov/library/stories/2019/02/fast-growth-in-desert-southwest-continues.html>). Rapid growth in the last two decades of the 20th century was coincident with one of the wettest periods of the last millennium<sup>4</sup>. The current drought, which began around 1998/99<sup>5,6</sup> is occurring in the presence of a large and growing population, an agriculture system that is a critical part of the US and global food supply and uses most of the region's surface water, and, due to rising greenhouse gases, a climate warmer than any in the history of water resource development. Warming increases atmospheric evaporative demand and can potentially reduce soil moisture and streamflows<sup>7–9</sup>. It can also dry vegetation and help explain the stark increases in burned forest areas in the West<sup>10</sup>. The confluence of an extended period of reduced precipitation and warming temperatures, rising population, and intensive agricultural water use are producing unprecedented stress on western agriculture and water resources (ref. <sup>11,12</sup>, <https://www.usbr.gov/newsroom/news-release/4294>), despite successful efforts to reduce water consumption. The expansion of forest fires only adds to the sense of a climate, resources and habitability crisis.

The obvious questions from both climatological and social impacts perspectives are: What is causing the drought? Is it natural variability, forced change or some mix? When will it end and what

will the future be like? In terms of human-induced change, warming will continue and climate models project a reduction in winter precipitation in Mexico and the far southwestern US and a robust drying across the West coast in spring<sup>13–15</sup> driven by enhanced dry zonal moisture advection<sup>16</sup>. However, in terms of natural variability, the wet period in the last two decades of the 20th century occurred in association with the warm tropical Pacific phase of the Pacific Decadal Oscillation (PDO)<sup>17–19</sup>, and the following 21st century megadrought has been related to the cool phase that began following the 1997/98 El Niño (e.g. <sup>6,20–23</sup>) thus illustrating the connection between the cool phase of the PDO and southwestern megadrought<sup>24</sup>. The Atlantic Multidecadal Oscillation (AMO), which has been in a warm phase since the mid-1990s, can also drive drought variability over western North America<sup>25–28</sup>. Therefore, past and future precipitation in the American Southwest depends on radiatively-forced change and how the PDO and AMO evolve.

Investigating decadal variability, forced change, and impacts on precipitation over land is not easy with state-of-the-art coupled models such as those within the Large Ensembles<sup>29</sup> and the latest generation Coupled Model Intercomparison Project 6<sup>30</sup>. Though some models can realistically simulate some aspects of the internally generated Pacific decadal variability<sup>31,32</sup>, others do not simulate the Pacific and Atlantic Oceans with high degrees of realism of spatial and temporal variability<sup>33,34</sup>. Even if models are able to simulate realistic internal decadal variability this would only line up in time with the observed variability by chance presenting challenges to model-data comparisons over the historical period. Further, the tropical Pacific Ocean exerts a strong control on North America cool season precipitation and it

<sup>1</sup>Lamont Doherty Earth Observatory of Columbia University, Palisades, New York, NY, USA. <sup>2</sup>Columbia Climate School, Columbia University, New York, NY, USA. <sup>3</sup>Physical Sciences Division, National Oceanic and Atmospheric Administration, Boulder, CO, USA. email: seager@ldeo.columbia.edu

appears possible that state-of-the-art models are misrepresenting its response to rising GHGs. The observed trend over past decades to a stronger zonal SST gradient across the equatorial Pacific and lack of warming in the cold tongue is at the very limit of, or beyond, the range of what models do when accounting for both their natural variability and forced response<sup>35–39</sup>. Hence in this work, to ensure realistic projections, we use an atmosphere model forced by SST variations due to the PDO and AMO that are empirically derived from observations (see Methods). These anomalies are added to a forced trend over the coming decades that is either (i) an extrapolation of the observed trend using regression to GHG forcing or (ii) the CMIP6 multimodel mean (Methods). These changes are added to a 1979 to 2018 observed SST climatology. This methodology ensures that the projections are relative to a real world climatology, have realistic natural decadal variability, and account for two very different scenarios of forced tropical Pacific SST change. These model experiments allow us to address the following questions: What are the middle-of-the-road, best-case, and worst-case scenarios for winter precipitation in the southwest accounting for forced change and decadal variability of the Pacific and Atlantic Oceans? What is the relative importance of forced change and decadal variability for future cool season precipitation in the southwest? Does the forced change depend on whether tropical Pacific SST trends continue as observed or switch over towards the El Niño-like changes seen in CMIP6 models? How important is cool season precipitation change for summer soil moisture change? Has human-driven climate change advanced such that the southwest will never return to the cool season precipitation and summer soil moisture amounts of the late 20th century?

## RESULTS

### Characterization and simulation of the 21st century megadrought

*Cool season precipitation during the 21st century megadrought.* Figure 1 characterizes the 21st century megadrought by showing the difference between the megadrought period of June 1998 to August 2021 and the pluvial period of January 1979 to May 1998 for SSTs, surface air temperature over land, geopotential heights in the upper troposphere, and precipitation. Despite ongoing global warming apparent over most land surfaces and oceans, there is a striking wedge-shaped region of cooling in the central to eastern tropical Pacific Ocean. This meridionally broad SST pattern is characteristic of ENSO-like Pacific decadal variability and has prior qualitative analogs in decadal shifts centered on 1946/47 and the 1976/77 El Niño<sup>40,41</sup>. There is a shift towards reduced precipitation above the tropical Pacific SST anomalies and low upper tropospheric geopotential heights throughout the tropics. There is also a shift towards an upper troposphere ridge that extends from the North Pacific over southern North America, characteristic of a La Niña teleconnection<sup>42,43</sup>. Consistently cool season precipitation is lower in the 21st century than in the late 20th century across much of southwestern North America. Figure 1c also shows 200hPa heights and precipitation differences from the ensemble mean of simulations with the atmosphere model forced by the observed SST history. The model simulates the shift to reduced precipitation over the tropical Pacific, the low heights in the tropics, the North Pacific to North America ridge, and the reduced precipitation over southwest North America. Since the ensemble mean isolates the forced variations in the atmosphere, of which the SST-forcing will be paramount, this demonstrates that the precipitation reduction within the 21st century megadrought was SST-driven. Prior experience with models that isolate the impacts of tropical Pacific forcing supports the idea that the driving for the megadrought is the tropical Pacific SST shift<sup>1,18</sup>. Figure 1d also shows the observed and modeled (ensemble mean and spread)

time series of cool season precipitation averaged over southwest North America. The model successfully simulates many wet and dry cool seasons as SST-forced (e.g. the 1982/83 and 1997/98 El Niños) and also reproduces the shift to overall drier conditions in the 21st century. The correlation coefficient between the observed and model ensemble mean cool season precipitation is 0.66 meaning that about a third of the year-to-year variability of cool season precipitation is driven by the ocean. Figure 1e shows box and whiskers diagrams of the modeled precipitation anomalies for the late 20th century and early 21st century decades and additionally marks the observed values. According to the model, the cross-ensemble spread of multidecadal average cool season precipitation in the two periods does not even overlap. The observed values for each period are at the outer edges of the model distribution. Collectively these results testify to a statistically significant role for the ocean in inducing a decadal shift in cool-season precipitation. Based on this model evidence of SST driving the megadrought, we expect that the future hydroclimate of the southwest will also be influenced by decadal variations of SST.

*Spring and summer soil moisture during the 21st century megadrought.* Figure 2 (top half) shows how this decadal shift towards drought is manifested in springtime (March to May) soil moisture and surface air humidity. Soil moisture declined across the entire region and was accompanied by a 10 to 20% decline in surface air humidity. The model simulated a similarly broad but weaker soil moisture reduction but only a weak surface air humidity reduction. The model and two observations-based products for soil moisture agree well on year-to-year variability and the decadal shift, including the absolute amplitude. For the shift, the NLDAS-2-NOAH product agrees with the model but the ERA5 shift is much larger. In the lower half of Fig. 2 we show the same for summer (June through August) soil moisture. Despite not simulating the reduction in summer precipitation (Fig. 1f), since this was probably not ocean-forced, the model still reasonably simulates the interannual variability and decadal shift in summer soil moisture as recorded by the NLDAS-2-NOAH product, though once more the ERA5 dry shift is much larger. These results strongly suggest summer soil moisture is heavily influenced on interannual to decadal timescales by cool season precipitation consistent with a prior analysis<sup>44</sup>.

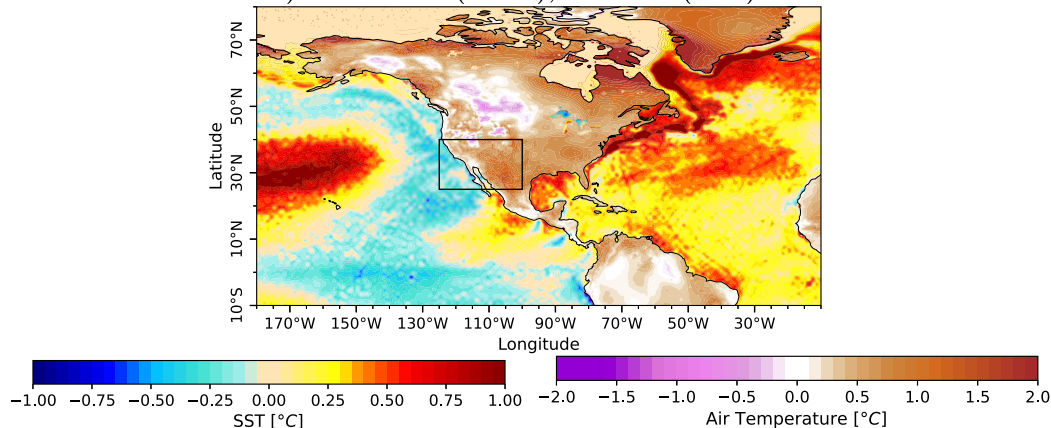
The controls on summer soil moisture can be elucidated by examining the relations across ensemble members of decadal changes in summer soil moisture, cool season precipitation, and summer surface air temperature and in observations-based estimates (Fig. 3). As noted before, there is a general negative association between surface air temperature and precipitation<sup>45,46</sup>. Summer soil moisture tracks cool season precipitation with the NLDAS-2 observational estimate well explained by the modeled relationship. (The ERA5 observational estimate has soils drier, precipitation lower, and air temperature higher than the model can simulate.) However, there is no apparent offset towards drier soils independent of changes in precipitation that would indicate an additional evaporative demand-driven drying. This is despite the clear summer warming that has occurred.

### Best-case and worst-case cool season precipitation outcomes for the next decade

Having demonstrated our modeling framework's ability to reproduce decadal variations in cool season precipitation and spring and summer soil moisture, we turn to its projections of the future and examine best and worst-case scenarios. Figure 4 shows the 2032–2041 cool season precipitation anomaly with respect to 1979 to 2021 as a function of PDO and AMO values for all members of the grand ensemble. Dry and wet conditions are

## DJFMAM Averages 1998-2021 - 1979-1998

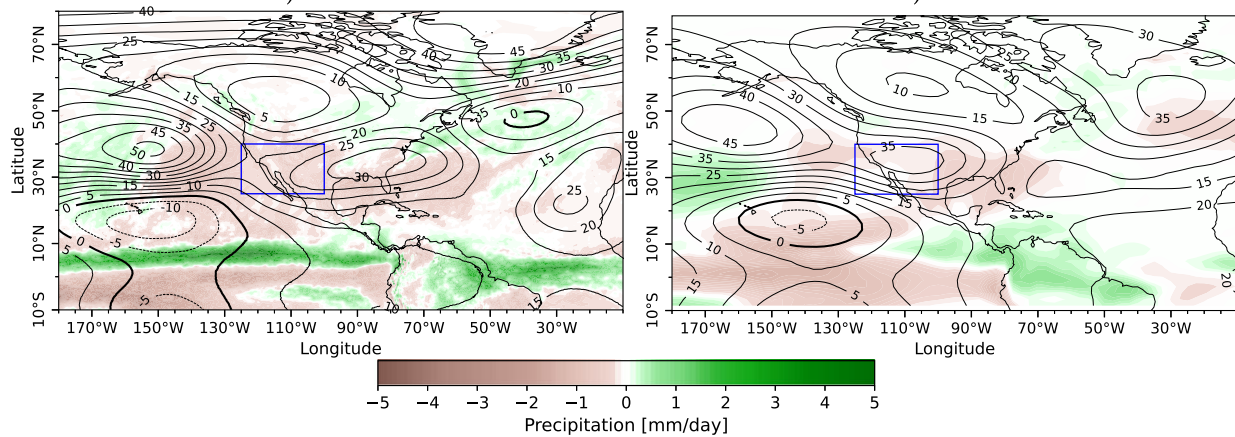
a) ERA5 SST (ocean), sfc air T (land)



Precipitation (color), Geopotential Height 200 hPa (contour)

b) ERA5

c) CAM6-LR



25N-40N, 125W-100W Land Only NOAA-CPC, CAM6-LR, ERA5

d) DJFMAM 1979-2021

e) DJFMAM 1979-1998, 1998-2021

f) JJASON 1979-1997, 1998-2020

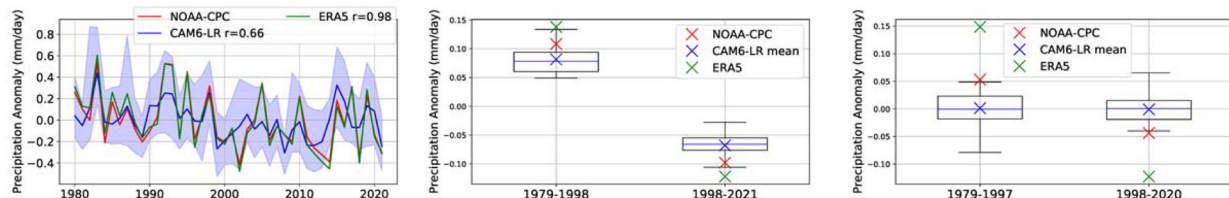


**Fig. 1 Observations and simulation of the 21st-century megadrought in southwest North America.** Shown are decadal changes between 1998 and 2021 and 1979 and 1998 in **a** ERA5 SST and surface air temperature (both in K) over ocean and land, respectively, precipitation (mm/day, colors) and 200 hPa heights (m, contours) for **b** ERA5 and **c** the CAM6-LR model, **d** time series of southwest cool season precipitation for NOAA-CPC observations, ERA5 and the CAM6-LR model simulation and box and whiskers plots for **e** cool and **f** warm season precipitation for 1979–1998 (left) and 1998–2021 (right) showing the CAM6-LR ensemble spread (box encloses 25th–75th percentiles, the horizontal line marks the median and the cross the mean with whiskers encompassing 99% of the distribution) with NOAA-CPC and ERA5 single values marked.

clearly related to the cool and warm tropical Pacific states of the PDO, respectively. Further, for any PDO state, precipitation is less if the AMO is positive. For reference, the model simulated precipitation anomalies for the 21st century megadrought and late 20th century pluvial are also shown along with the observed values (these all have single values for the AMO and PDO). The future projections are consistent with the historical influences of the PDO and AMO on cool season precipitation in models and observations. (The historical modeled and observed values are for 20-year averages and hence the lower magnitude compared to the 10-year average projections is to be expected.) The worst case scenario is negative PDO, positive AMO - denoted PDO+AMO+

with the same notation for other mode combinations - and the best case is PDO+AMO-. This is consistent with prior work<sup>47</sup>. The separate effects of the PDO and AMO on future climate are shown in Fig. 5 (see Methods for how quantified). A cool tropical Pacific suppresses precipitation and forces an anomalous high over the North Pacific and southern North America that deflects the Pacific storm track and jet stream northward (Fig. 5a-d, ref. <sup>18</sup>) and induces subsidence over the southwest. A warm tropical Atlantic suppresses precipitation over the tropical Pacific forcing a similar but weaker Rossby wave response to the North Pacific and North America and also induces anticyclonic circulation over the

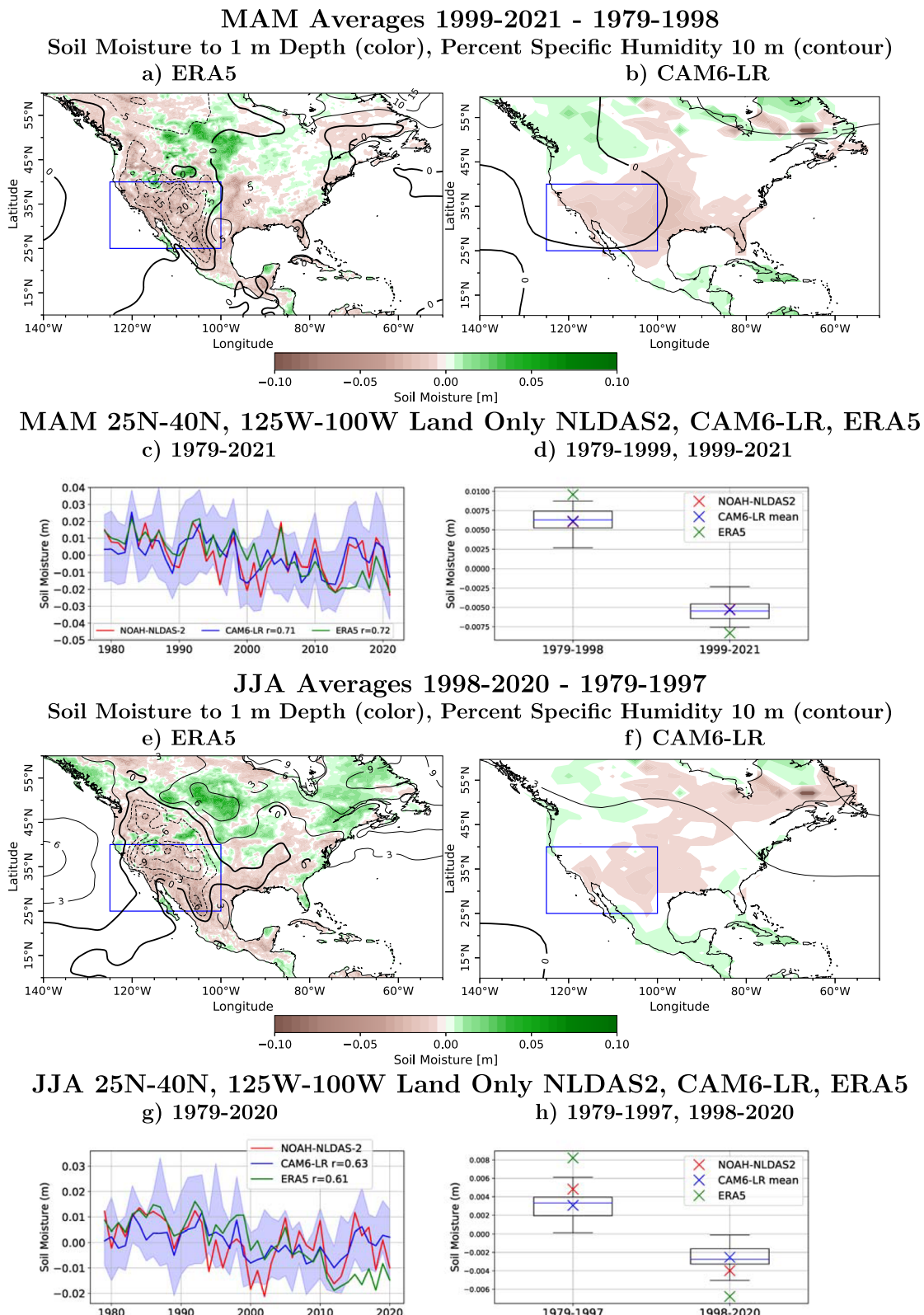


**Fig. 2 Spring and summer soil moisture during the 21st-century megadrought.** The (1999–2021) minus (1979–1998) decadal shift in spring soil moisture and surface specific humidity in **a** ERA5 and **b** the CAM6-LR model simulation, the time series of spring soil moisture in the southwest in the NLDAS-2 land data assimilation product, ERA5, and the CAM6-LR model simulation and **d** box and whiskers plots of spring soil moisture for the CAM6-LR ensemble (boxes enclose the 25th–75th percentile, the horizontal line marks the median and the cross the mean and the whiskers encompass 99% of the data) with NLDAS-2 and ERA5 single values marked for 1979–1998 (left) and 1998–2021 (right). **e–h** as for **a–d** but for summer. The blue box shows the southwest region for all land-only area averages. Units are m for soil moisture and percent of climatology for humidity.

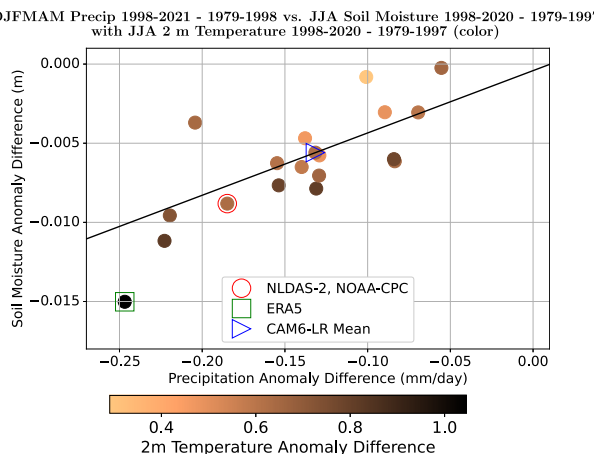


**Fig. 3 The relation between summer soil moisture and temperature and cool season precipitation.** The relation across ensemble members between the (1999–2021) minus (1979–1998) decadal shifts in summer soil moisture (m, y-axis), cool season precipitation (mm/day, x-axis), and surface air temperature (K, color of dots with color bar below). Each dot is an ensemble member with the ensemble mean marked by the rightwards-pointing blue triangle. Observations-based products from ERA5 (green square) and NLDAS-2 (red circle) are also marked. The black line is a linear least squares fit to the CAM6-LR ensemble members.

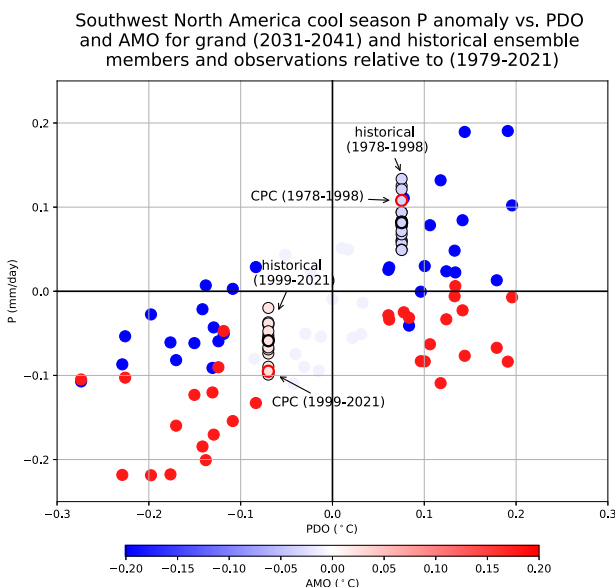


**Fig. 4 Dependence of cool season precipitation on the PDO and AMO.** Shown are values for all members of the grand ensemble for 2031–2041 minus 1979 to 2021. Also shown and labeled are the values for the ensemble members for the historical ensemble for both 1999–2021 and 1979–1998 minus 1979–2021. For the historical ensemble forcing by observed SST means the PDO and AMO values are the same for each ensemble member. Also shown are observed values as labeled. Units for precipitation are mm/day, K for the AMO, and standardized for the PDO.

southern U.S. and Gulf of Mexico with northerly, descending and drying flow over the southwest Fig. 5e–h, ref. <sup>27</sup>.

Figure 6 shows maps of cool season precipitation and 200hPa heights for the next decade, 2032–2041, relative to the historical 1979 to 2021 period. The worst-case scenario, with either Hadley or CMIP-based SST trend (Fig. 6b, e), shows classic signals of a cool tropical Pacific and warm tropical North Atlantic<sup>27,47</sup> with a decline of precipitation over the equatorial Pacific, straddling cyclones

aloft, anomalous highs over the North Pacific and southern U.S. and precipitation reduced across the North Pacific and all of southern North America and increased over the Caribbean and southern Central America. The high pressure over the North Pacific is contributed to by a response to the trends in SST and GHGs as seen in the grand ensemble mean across all modes of variability (Fig. 6g, f). As a result, in the best-case scenario (PDO+AMO-, Fig. 6a, d) despite regions of enhanced precipitation in the tropical Pacific, there is no trough over the North Pacific, and with the Hadley-based trend there remains an anomalous high. This prevents the best-case state of climate modes from providing a consistent region-wide increase in cool season precipitation. The difference between the worst and best-case scenarios for both SST-forcing scenarios (Fig. 6c, f) is clear: drier conditions over the southwest (order of 0.3 mm/day) connected to a high that is teleconnected from tropical SST and precipitation differences. Since the mean cool season precipitation in the model is on the order of a realistic 1mm/day<sup>6</sup>, this represents a quite large dependency on decadal ocean variability.

### The forced response in cool season precipitation and its dependence on tropical Pacific SST trends

Averaging across the entire large ensemble (comprising the PDO +AMO-, PDO–AMO+, PDO+AMO+, PDO–AMO–, PDOnAMON ensembles) will reduce the influence of modes of variability relative to the forced SST trends. The grand ensemble means ("All") are shown in Fig. 6g–i for the CMIP6 and Hadley-based SST trends. The Hadley-based SST trend leads to reduced precipitation along the equator in the Pacific, consistent with the lack of warming in the cold tongue, straddling upper troposphere cyclones in the subtropical Pacific and a high over the North Pacific and another over the south-central United States. The CMIP6-based SST trend leads to more diffuse tropical Pacific precipitation anomalies and a much weaker North Pacific high. The Hadley-based precipitation and circulation anomalies are notably similar to those of the PDO –AMO+ combination alone. This is because the Hadley SST trend by having relative cooling in the equatorial Pacific can influence local precipitation in a way akin to the negative (cool tropics) phase of the PDO. Further, the background forcing creates a tendency to a North Pacific high as seen in the ensembles with neutral states of the PDO and AMO (Fig. 6j–l). The average of the neutral-neutral ensemble members (Fig. 6j–l) looks like the All grand ensemble (Fig. 6g–i) which rules out any large nonlinear response of cool season precipitation and heights to the modes of SST variability.

### Dependence of summer soil moisture futures on cool season precipitation and background warming

For the historical period, the 21st century megadrought in summer soil moisture decline was driven by the cool season precipitation decline. Does this cross-seasons hydroclimate connection remain the case for future projections under greater radiative forcing and warming? Fig. 7 shows that it does. In the top row, we show the time series of modeled cool season precipitation for the historical simulations and the best (PDO+AMO–) and worst (PDO–AMO+) case scenarios with both CMIP6 (wetter) and Hadley (drier) forced SST trends. The separation between these scenarios for the future makes clear the continued importance of decadal variability. This is also shown in the bottom row of Fig. 7 where the driest (with Hadley) and wettest (with CMIP6) scenarios' ensemble spreads for cool season precipitation do not overlap. By contrast, for these scenarios, the summer precipitation overlaps, and the PDO–AMO+ with Hadley-based forced SST scenario is slightly the wetter of the two. Nonetheless, the JJA soil moisture reflects the dry and wet separation inherited from the cool season precipitation, and, again, the ensemble spreads do not overlap. The very best case returns summer soil moisture to the 1979 to 2021 climatology while the worst case scenario is dry with no

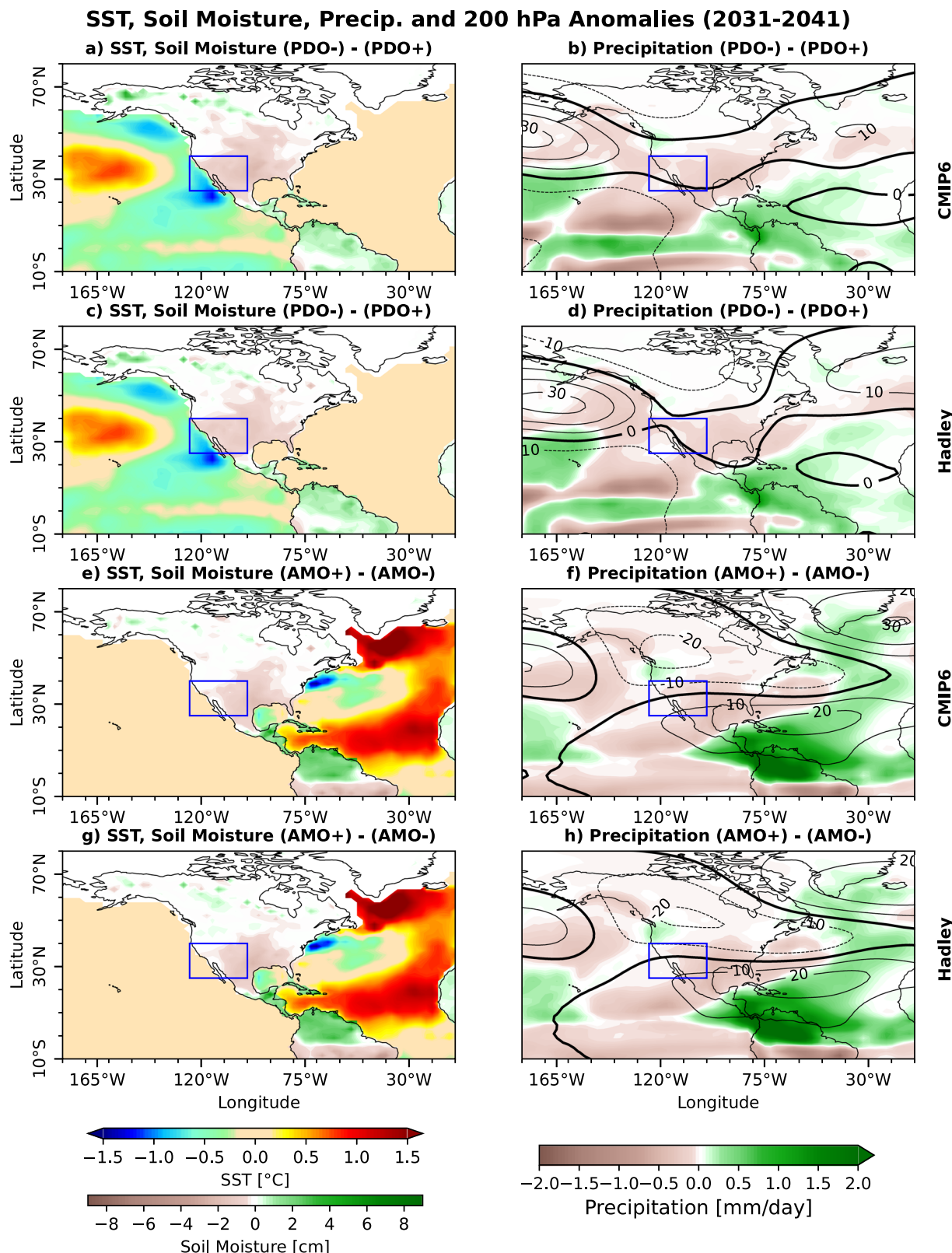


**Fig. 5 The separate effects of the PDO and AMO on precipitation, soil moisture and circulation.** Shown in the left column (**a, c, e, g**) are the SST anomalies (ocean) and the soil moisture response (land) and at the right (**b, d, f, h**), the precipitation (colors) and 200 hPa heights (contour) responses. Results are shown for both the grand ensembles with Hadley and CMIP6-based forced SST trends. Units are K for SST, m for heights, mm/day for precipitation, and cm for soil moisture.

## DJFMAM precipitation and 200 hPa anomalies (2031–2041) – (1979–2021)

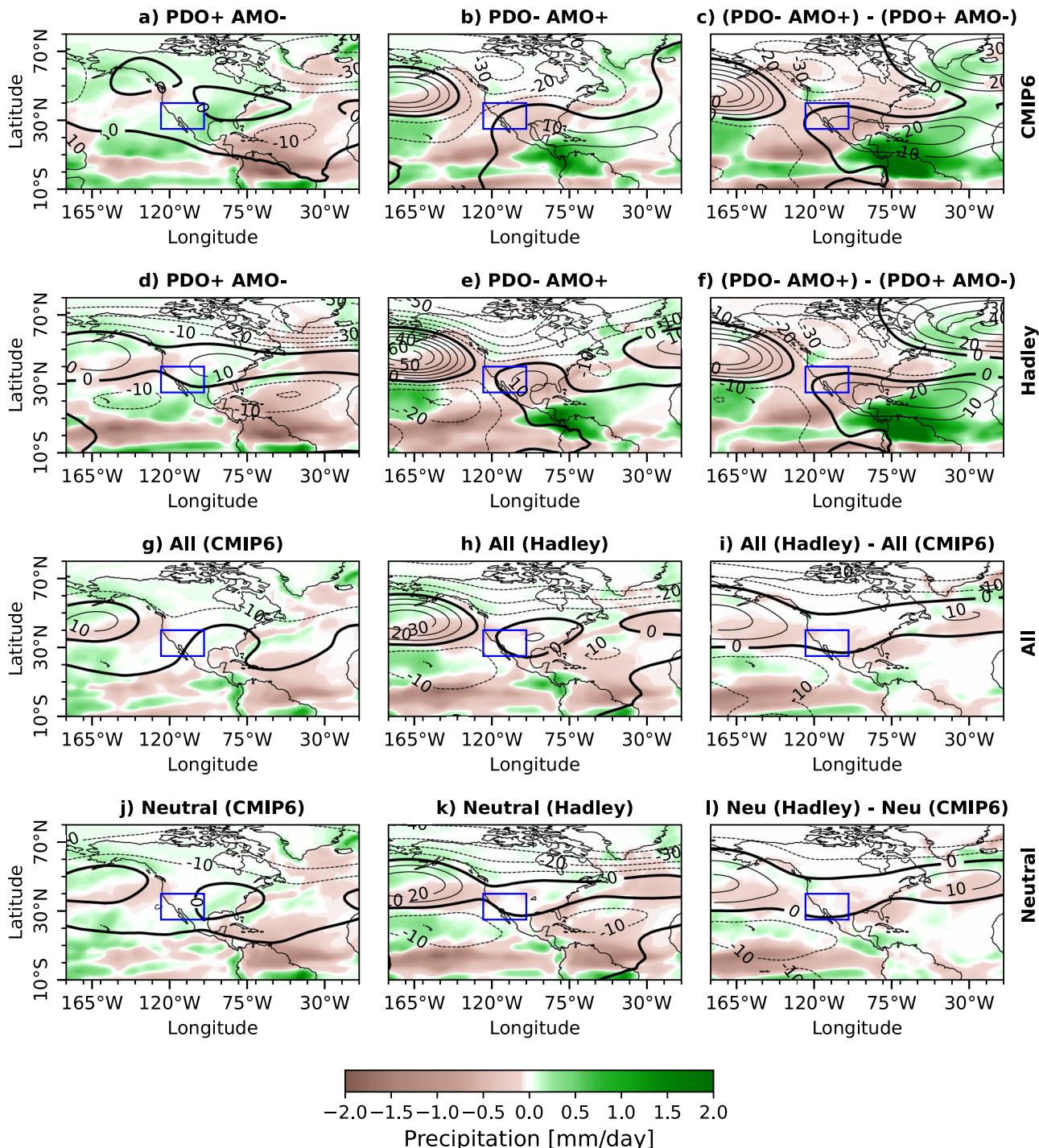


**Fig. 6 Best and worst cases for future cool season precipitation.** Colors are for precipitation (mm/day) and contours for 200h Pa heights with area-weighted global mean removed (m). The top row shows the case with CMIP6-based SST trend and, in the left column, the best case of a positive PDO and negative AMO (a, d); the middle column, the worst case of a negative PDO and positive AMO (b, e) and, in the right column, the worst case minus best case (c, f). The second row is as for the top row but with the case of Hadley-based SST trend. The third row (g–i) shows the grand ensemble mean, which averages across all modes of SST variability to isolate the SST-trend and radiatively forced response for, left, the CMIP6-based and, center, the Hadley-based SST trend and, right the Hadley minus CMIP6 difference. The bottom row (j–l) is as for the third row but averages across only the neutral PDO and AMO ensemble.

ensemble members even reaching the 1979–2021 average level of moisture. However, human-induced drying of soils in summer is also apparent in the next decade. The grand-ensemble summer soil moisture anomalies are shown at the bottom of Fig. 7. With

the CMIP6 SST trend forcing 75% of ensemble members are drier than the historical average and with Hadley SST trend forcing between 75 and 95% are drier. Some of this is due to a human-induced decline in precipitation (Fig. 7) which is greater with the

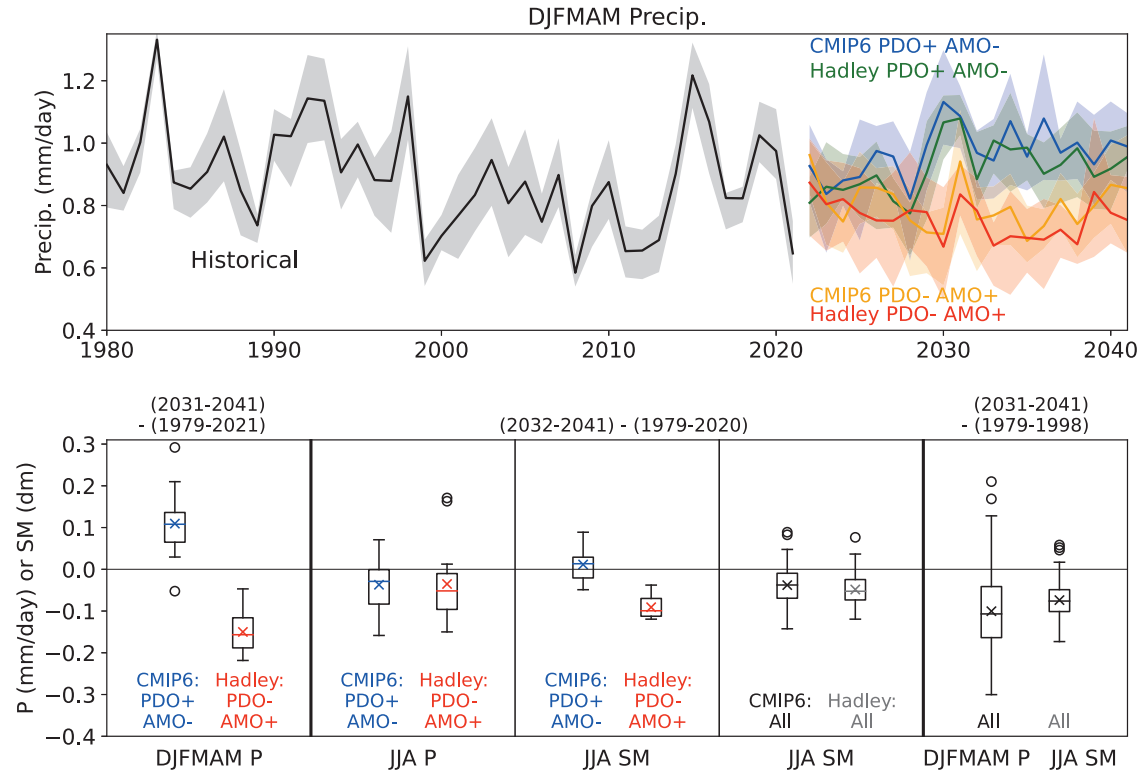


**Fig. 7 Future precipitation and soil moisture evolution in the context of the late 20th-century pluvial and 21st-century megadrought.** Top: time series of cool season precipitation in the southwest from the CAM6-LR historical ensemble for 1979–2021 with 2022–2041 projections for the best-case (PDO+AMO−) and worst-case (PDO−AMO+) decadal SST scenarios and both the Hadley- and CMIP6-based forced SST trends. Bottom: the left three panels show box and whiskers plots (boxes enclose the 25th–75th percentiles, the horizontal line marks the median, the cross the mean and whiskers encompass 99% of the distributions) of anomalies of cool season precipitation, summer precipitation, and summer soil moisture for the best and worst case decadal SST variations and, in the fourth panel, the summer soil moisture for the grand ensemble including all modes of decadal SST variation. Anomalies are relative to 1979–2021 for cool season precipitation and 1979–2020 for summer values. The bottom right box and whiskers show the distributions across the two grand ensembles of cool season precipitation and summer soil moisture relative to the late 20th-century pluvial (DJFMAM 1979–1998 and JJA 1979–1997). Units for precipitation are mm/day and for soil moisture are decimeters.

Hadley-based than CMIP6-based SST trend. However, the difference between the JJA soil moisture trends between the two ensembles is modest and the drying common to both indicates an additional drying due to the common atmospheric warming. Further, the distribution across both grand ensembles for cool season precipitation and summer soil moisture indicates a high probability of moisture levels never returning to those of the late 20th-century pluvial (Fig. 7, bottom right).

## DISCUSSION

The ongoing 21st century megadrought is attributed to a decline in cool season precipitation that dries soils into summer. Any additional influence of warming over the most recent decades on reducing summer soil moisture is not clear compared to precipitation-induced drying. Prior work has drawn attention to the role of human-driven warming in contributing to the 21st century megadrought<sup>4</sup> although adopting a longer-term perspective and not explicitly evaluating the impact of the observed strong decadal shift in precipitation from the late 20th to early 21st century. Our results make clear the dominant influence on the 21st-century megadrought of circulation and precipitation anomalies driven by decadal variations of sea surface temperatures. The influence of ocean variability remains potent for the next two decades. In the worst-case scenario with a persistent cool tropical Pacific state and a warm tropical Atlantic, the megadrought will persist. In the best-case scenario with a warm tropical Pacific and a cold tropical Atlantic state, there will be significant abatement and even an end to the

megadrought. However, even in this scenario the cool season precipitation and summer soil moisture will most likely not return to the levels seen at the end of the 20th century (Fig. 7, bottom right). In terms of the radiatively-forced response, drying, in terms of both cool season precipitation and summer soil moisture, is enhanced modestly if tropical SSTs continue to show no warming of the equatorial Pacific cold tongue rather than if the cold tongue warms as in the CMIP6 ensemble mean. The future human-driven drying is driven both by a reduction in cool season precipitation and warming that enhances evaporative demand and dries soils. It has long been established that the modern drought history of the southwest has been driven by circulation and precipitation variations that are themselves forced to an important extent by SST variations with the tropical Pacific the most important ocean region<sup>1,2,24,49</sup>. However, as human-driven warming has accelerated, more attention has shifted to how evaporative demand-driven drying of soils can enhance drought risk<sup>4,7,50,51</sup>. Here we show that for the next two decades for which planning decisions are being made today, cool season precipitation variations driven by modes of SST variability will remain important, even dominant, in setting the hydroclimate future of the southwest. Our ability to predict tropical Pacific decadal variability, and its association with inter-basin interactions, remains limited on the decadal timescales<sup>33,52–54</sup>. Hence, it appears likely it will not be possible to advise those charged with adapting to climate whether the southwest will experience the worst-case, best-case or some intermediate scenario in coming decades. In addition, we are still not in a position to know whether, in response to rising greenhouse gases, the cold tongue will continue to not warm up, or

whether it will transition into warming<sup>55</sup> and this also introduces uncertainty in hydroclimate projections for the southwest. However, we can be sure that local warming in the Southwest will continue. While we do not see that local warming to date has drawn down summer soil moisture significantly this signal does appear in the next decade and becomes comparable to the influence of modes of climate variability. As such, according to our simulations, even the best-case scenario with a warm tropical Pacific, cool tropical North Atlantic, and cold tongue warming will not lift cool season precipitation and summer soil moisture back to the levels of the late 20th century before the onset of the 21st-century megadrought. The long-predicted aridification of the American Southwest<sup>56</sup> is underway and fortuitous decadal climate variability will be insufficient to stop it.

## METHODS

### Observational and observations-based data

For the observational analyses of the historical period we use the following data. For precipitation over land and sea we use the National Oceanic and Atmospheric Administration (NOAA) Climate Prediction Center (CPC) Unified combined satellite and gauge data at 0.5° resolution provided by the NOAA Office of Atmospheric Research Earth System Research Laboratory Physical Sciences Division, Boulder, Colorado, USA, and obtained from the International Research Institute for Climate and Society (IRI) at [http://iri.ideo.columbia.edu/SOURCES/NOAA/NCEP/CPC/UNIFIED\\_PRCP/GAUGE\\_BASED/GLOBAL/v1p0/index.html](http://iri.ideo.columbia.edu/SOURCES/NOAA/NCEP/CPC/UNIFIED_PRCP/GAUGE_BASED/GLOBAL/v1p0/index.html)<sup>57</sup>. For sea surface temperature, surface air temperature over land, precipitation over land and sea, surface air humidity and geopotential heights we use the European Centre for Medium Range Weather Forecasts (ECMWF) Reanalysis Five (ERA5, ref. <sup>58</sup>). For soil moisture we use values for the top 1 m from ERA5 and the NLDAS-2 Noah land assimilation data (<https://disc.gsfc.nasa.gov/datasets?keywords=NLDAS>). All data cover January 1979 to August 2021 to match the atmosphere model simulations.

### Atmosphere-land model

For the historical period and the future, we use an atmosphere-land model forced by imposed SSTs. The atmosphere model is a low resolution (2° × 2°, 32 levels) version of the current NCAR Community Atmosphere Model 6<sup>59,60</sup>, run in “-chem none” mode which disables prognostic aerosols, and is denoted CAM6-LR. This model version was created by us to be more computationally efficient than the standard version of CAM6 and allow us to generate large ensembles of projections using in-house computing. The atmosphere model is coupled through energy and water fluxes at the surface to the Community Land Model (CLM). CLM computes the modeled soil moisture analyzed here.

### Historical simulations ensemble

For the historical period, CAM6-LR was forced by the “blended” SST data created by NCAR<sup>61</sup> which blends Hadley Center’s HadISST1.1 data from 1870 on with the NOAA Optimal Interpolation version 2 data from November 1981 onward. The model was additionally forced by the standard set of CMIP6 forcings used for Community Earth System Model 2 with changing trace gases, solar variability, stratospheric aerosols and land use/land cover change to 2014<sup>62</sup>, with the exception of aerosols outside of the stratosphere, where climatologically varying present-day (1995–2005) concentrations were used in conjunction with the less computationally expensive bulk aerosol scheme, and the SSP370 scenarios thereon to 2021. For the historical period, we generate 16 ensemble members with each member initiated on January 1, 1979 with the final state of a one-year climatological spin up simulation with perturbed initial conditions.

### Future projections ensemble

For future projections, we generate a boundary-forced ensemble in which each ensemble member is forced with a different sequence of PDO and ENSO variability, but the same AMO variability, all as generated by the LIM (see details below). SST forcings are selected to cover the following combinations of PDO and AMO: PDO+AMO+, PDO-AMO-, PDO+AMO-, PDO-AMO+, PDOnAMOn, where the latter refers to neutral states, giving a total of 80 simulations referred to as ‘All’ or ‘grand ensemble’. One grand ensemble is generated for the Hadley-based SST trend and one for the CMIP6 SST trend. The projection ensemble members additionally experience changes in radiative forcing and land use/land cover consistent with the CMIP6 SSP370 scenarios. Ensemble members are initialized in their atmosphere and land states as continuations of the historical ensemble members. The SST forcing and simulation data are available at <http://hodges.ideo.columbia.edu:81/expert/SOURCES/.CAM6/.forRichard/.CAM6>.

### Definition of Southwest region

The southwest region is defined as 25°N to 40°N, 125°W to 100°W, land only. An area-weighted average over this area is used. The area is shown as a blue box in Figs. 2, 5, and 6.

### Construction of SST forcing fields

*PDO, AMO, and ENSO.* We use a linear inverse model (LIM) to generate ensembles of possible SST scenarios of natural variability that share similar characteristics to the historical observations for the period 1958–2017. To better represent the seasonal cycle in the SST data, we use the cyclostationary linear inverse model (CSLIM) in this study (e.g. <sup>63,64</sup>). More details about the LIM and CSLIM methods can be found in previous studies<sup>63–67</sup>. Briefly, both LIM and CSLIM assume that the slowly evolving (long time scale) dynamics of the coupled ocean-atmosphere system can be approximated as linear and the role of the fast nonlinear processes can be approximated as Gaussian noise on the slow time scales:

$$\frac{d\mathbf{X}}{dt} = \mathbf{L}\mathbf{X} + \zeta \quad (1)$$

where  $\mathbf{X}$  is the system state vector,  $\mathbf{L}$  is the linear dynamical system matrix, and  $\zeta$  is the (spatially coherent) white noise forcing. For a standard “stationary” LIM model,  $\mathbf{L}$  is constant in time. In the CSLIM, the seasonally varying dynamical system matrices  $\mathbf{L}^{month}$  are calculated separately for each month, thus twelve different  $\mathbf{L}$  matrices are constructed based on observational data. Similarly, the spatial structure of the white noise forcing also varies for each month.

The state vector  $\mathbf{X}$  in (1) consists of the nine leading principal components (PCs; 79% variance explained) of global SST from the HadISST dataset<sup>68</sup> for the period 1958 to 2017. To separate the secular trend from the natural variability, a stationary LIM was first computed. The trend is then determined from the least damped eigenmode of the stationary LIM, which is subsequently removed from the original data<sup>69,70</sup>. After this step, we re-computed CSLIM where the  $\mathbf{L}$  matrix varies each month. Then we integrated CSLIM forwards<sup>71</sup> to generate the synthetic SST data used here. Each realization may be considered to be an “alternative history” of natural SST variability that could have happened over the past sixty years since its spatiotemporal evolution is statistically consistent with past observations<sup>72,73</sup>. A total of 100 members of the 60-year synthetic SST evolutions were generated. These 6000 years of synthetic SST form the basis of the possible PDO/AMO state selection.

In selecting the possible PDO and AMO states for 2020 to 2041, we first subdivide the 6000-year SST data into 21-year chunks with a moving 5-year window (e.g., 1–21, 6–26, 11–31, etc.). This allowed us to obtain 800 members of 21-year average

SST. We then selected the top 120 members with the strongest 21-year average PDO+ and PDO- index (defined based on the projection to the first Empirical Orthogonal Function mode of the North Pacific SST, north of 20°N for the 6000 years of LIM-simulated SST). To keep the naturally varying ENSO cycle, we selected from the top 120 members the (i) 16 members of PDO+ and (ii) the 16 members of PDO- that share similar PDO temporal evolution (evaluated by temporal correlation between the like sign PDO members). Since the PDO and ENSO vary over time in these SST histories we additionally require that the selected members do not have a strong 21-year trend from natural variability. This avoids interference of the modes of variability with the separately-imposed anthropogenic forced SST trend. The temporal evolutions of each of the 16 PDO+/PDO- members and the average PDO SST patterns over the North Pacific are shown in Supplementary Material Fig. 1. These 16 members of the 21-year PDO+/PDO- SST evolution contain random ENSO cycles that mimic what happens in the real world. The AMO is defined as the area average SST over the North Atlantic Ocean 0–60°N. For the AMO mode selection, we choose from the 21-year segments with the maximum positive AMO amplitude for AMO+ and the most negative index for AMO-. The temporal evolution and the SST patterns are shown in Supplementary Material Fig. 2. The neutral PDO are chosen based on the 16 members that have the PDO index closest to zero and, once more, do not contain a strong natural variability trend over the 21 years. The neutral AMO is selected from the member with AMO amplitude closest to zero.

**Radiatively-forced SST trend.** The PDO, AMO and ENSO SST variability is added to estimates of the forced SST trend due to increased radiative forcing. For one grand ensemble, the 2021 to 2041 forced SST trend for each calendar month is computed as the multimodel mean of 40 CMIP6 models forced with the SSP370 emissions scenario [http://kage.ldeo.columbia.edu:81/SOURCES/.LDEO/.ClimateGroup/.PROJECTS/.SST/reference\\_datasets/.CMIP6\\_historical-ssp370\\_ts.nc/](http://kage.ldeo.columbia.edu:81/SOURCES/.LDEO/.ClimateGroup/.PROJECTS/.SST/reference_datasets/.CMIP6_historical-ssp370_ts.nc/). For the other ensemble we extrapolate the observed SST trend using HadISST data<sup>68</sup>. For the observational record from 1900 to 2020 we regress the SSTs for each calendar month across years onto a time series of total GHG forcing from <https://live.magicc.org> as used in CMIP6<sup>74</sup>. The future forced SST trend is then computed using these monthly regression coefficients and projected total GHG forcing for 2021 to 2040 from <https://live.magicc.org> which is consistent with the CMIP6 SSP370 scenario.

**Construction of total SST forcing fields.** The total SST fields used to force the atmosphere model are constructed by adding the monthly SST variations due to the PDO, AMO, and ENSO and the monthly Hadley or CMIP6-based forced trends to a 1979 to 2018 HadISST monthly climatological SST field. Note that by construction the PDO and ENSO are different in each ensemble member for each PDO, AMO combination ensemble. Hence, we refer to this as an SST-forced boundary-value large ensemble.

**Patterns of SST change.** Supplementary Material Figure 3 shows the difference in near-global SST for DJFMAM of 2032–2041 minus 1979–2021 to complement the changes in heights and precipitation for these same periods shown in the main paper. Shown are the differences for the PDO+AMO-, PDO-AMO+, and the grand ensemble (All) with CMIP6 and Hadley-based SST trends. Use of the observed SST state, containing forced and natural variation components, for the reference period, makes SST, height, and precipitation changes in 2032–2041 distinct from those that would be seen in a fully coupled CMIP6 ensemble in which the earlier period is also model generated with the natural variability typically filtered through cross-ensemble averaging.

## Identification of separate effects of PDO and AMO

We can use sums and differences of the sub-ensembles to identify the separate effects of the PDO and AMO on precipitation, soil moisture and 200hPa heights. To identify the impact of the PDO we perform on any model quantities the operation  $(\text{PDO-AMO-} + \text{PDO-AMO+}) / 2 - (\text{PDO+AMO+} + \text{PDO+AMO-}) / 2$ . This removes the impact of the AMO to isolate the impact of the PDO measured as PDO- minus PDO+. Similar operations are carried out to isolate the AMO impact as AMO+ minus AMO-.

## Separation into 20th century pluvial and 21st century megadrought and future minus past differences

We divide the historical period into a late 20th century pluvial and a 21st century megadrought. The driver for this transition is considered to be the tropical Pacific Ocean. After the 1997/98 El Niño, the equatorial Pacific shifted towards cooler than normal SSTs in May–June 1998. We, therefore, chose December 1979 to May 1998 as the 20th century pluvial and June 1998 to August 2021 as the 21st century megadrought. In almost all analyses future values are plotted relative to the December–May 1979–1980 to December–May 2020–2021 and June–August 1979 to 2020 climatologies. For comparing to the late 20th century pluvial the December–May 1979–1980 to December–May 1997 and June–August 1979 to June–August 1997 climatologies are the reference period. For future time we use December–May 2031–32 through December–May 2040–2041 and June–August 2032 through June–August 2041. In the future minus past differences, it should be noted that the earlier period is a model simulation forced by historical SSTs. Since the SSTs in this period are different from those in coupled CMIP models the differences in SSTs, heights and precipitation shown here are also different from those that would be seen within CMIP models alone. In particular, the future trend toward a deeper North Pacific Low<sup>75,76</sup> is not seen when the model is forced with CMIP6 SST trend out to 2041 is added to the observed SST climatology. The projected low has been causally connected with enhanced eastern equatorial Pacific warming but we hypothesize that when this aspect of the CMIP6 SST trend is added to an observed state in which the eastern equatorial Pacific has not warmed it is insufficient to generate locally enhanced convection and an El Niño-like teleconnection<sup>76</sup>.

## DATA AVAILABILITY

The observational, observations-based and model simulation data, including forcing data, are available at the links provided in the relevant subsections in the Methods section.

## CODE AVAILABILITY

The atmosphere model simulations were performed with National Center for Atmospheric Research Community Atmosphere Model 6 for which the code can be accessed at <https://www.cesm.ucar.edu/models/cesm2/atmosphere>. Code for the Linear Inverse Model to generate sea surface temperature projections is available upon request. Analysis of observations, reanalyses and the model simulations and figures were generated using the python matplotlib (<https://matplotlib.org>), numpy (<https://numpy.org>), pandas (<https://pandas.pydata.org>), xarray (<https://docs.xarray.dev/en/stable/>) and cartopy (<https://scitools.org.uk/cartopy/docs/latest/>) libraries and codes will be made available upon request to the authors.

Received: 19 April 2023; Accepted: 18 August 2023;  
Published online: 14 September 2023

## REFERENCES

1. Seager, R., Kushnir, Y., Herweijer, C., Naik, N. & Velez, J. Modeling of tropical forcing of persistent droughts and pluvials over Western North America: 1856–2000. *J. Clim.* **18**, 4068–4091 (2005).

2. Cook, E. R., Woodhouse, C., Eakin, C. M., Meko, D. M. & Stahle, D. W. Long term aridity changes in the western United States. *Science* **306**, 1015–1018 (2004).
3. Cook, E. R., Seager, R., Cane, M. A. & Stahle, D. W. North American droughts: reconstructions, causes and consequences. *Earth. Sci. Rev.* **81**, 93–134 (2007).
4. Williams, A. P. et al. Large contribution from anthropogenic warming to an emerging North American megadrought. *Science* **368**, 314–318 (2020).
5. Seager, R. The turn-of-the-century North American drought: dynamics, global context and prior analogues. *J. Clim.* **20**, 5527–5552 (2007).
6. Seager, R. et al. Mechanisms of a meteorological drought onset: summer 2020 to spring 2021 in southwestern North America. *J. Clim.* **35**, 3767–3785 (2022).
7. Diffenbaugh, N. S., Swain, D. L. & Touma, D. Anthropogenic warming has increased drought risk in California. *Proc. Nat. Acad. Sci.* **112**, 3931–3936 (2015).
8. McCabe, G. J., Wolock, D. M., Pederson, G. T., Woodhouse, C. & McAfee, S. Evidence that recent warming is reducing Upper Colorado River flows. *Earth Int.* **21**, 1–14 (2017).
9. Xiao, M., Udall, B. & Lettenmaier, D. P. On the causes of declining Colorado River streamflows. *Water Resour. Res.* **54**, 6739–6756 (2018).
10. Abatzoglou, J. T. & Williams, A. P. Impact of anthropogenic climate change on wildfire across western US forests. *Proc. Nat. Acad. Sci.* **113**, 11770–11775 (2016).
11. Dettinger, M. D., Udall, B. & Georgakakos, A. Western water and climate change. *Ecol. Appl.* **25**, 2069–2093 (2015).
12. Pathak, T. et al. Climate change trends and impacts on California agriculture: a detailed review. *Agronomy* **8**, 25 (2018).
13. Gao, Y. et al. Robust spring drying in the Southwestern US and seasonal migration of wet/dry patterns in a warmer climate. *Geophys. Res. Lett.* **41**, 1745–1751 (2014).
14. Maloney, E. D. et al. North American climate in CMIP5 experiments: Part III: assessment of 21st century projections. *J. Climate* **27**, 2230–2270 (2014).
15. Cook, B. et al. Twenty-first century drought projections in the CMIP6 forcing scenarios. *Earth's Future* **8**, e2019EF001461 (2020).
16. Ting, M., Seager, R., Li, C., Liu, H. & Henderson, N. Mechanisms of future spring drying in the southwestern United States in CMIP5 models. *J. Clim.* **31**, 4265–4279 (2018).
17. Power, S., Casey, T., Folland, C., Colman, A. & Mehta, V. Interdecadal modulation of the impact of ENSO on Australia. *Clim. Dyn.* **15**, 319–324 (1999).
18. Huang, H., Seager, R. & Kushnir, Y. The 1976/77 transition in precipitation over the Americas and the influence of tropical SST. *Clim. Dyn.* **24**, 721–740 (2005).
19. Meehl, G. A., Hu, A., Santer, B. & Xie, S. Contribution of the Interdecadal Pacific Oscillation to twentieth century global surface temperature trends. *Nat. Clim. Ch.* **6**, 1005–1008 (2016).
20. Hoerling, M. P., Eischeid, J. & Perlitz, J. Regional precipitation trends: distinguishing natural variability from anthropogenic forcing. *J. Clim.* **23**, 2131–2145 (2010).
21. Delworth, T., Zeng, F., Rosati, A., Vecchi, G. A. & Wittenberg, A. T. A link between the hiatus in global warming and North American drought. *J. Clim.* **28**, 3834–3845 (2015).
22. Lehner, F., Deser, C., Simpson, I. R. & Terray, L. Attributing the U.S. Southwest's recent shift into drier conditions. *Geophys. Res. Lett.* **45**, 6251–6261 (2018).
23. Kumar, S., Dewes, C. F., Newman, M. & Duan, Y. Robust changes in North America's hydroclimate variability and predictability. *Earth's Future* **11**, e2022EF003239 (2023).
24. Meehl, G. & Hu, A. Megadroughts in the Indian monsoon region and Southwest North America and a mechanism for associated multidecadal Pacific sea surface temperature anomalies. *J. Clim.* **19**, 1605–1623 (2006).
25. McCabe, G. J., Palecki, M. A., Gray, S. & Betancourt, J. L. Pacific and Atlantic influences on multidecadal drought frequency in the United States. *PNAS* **101**, 4136–4141 (2004).
26. McCabe, G. J., Betancourt, J. L., Palecki, M. A. & Hidalgo, H. Association of multidecadal sea surface temperature variability with US drought. *Quat. Int.* **188**, 31–40 (2008).
27. Kushnir, Y., Seager, R., Ting, M., Naik, N. & Nakamura, J. Mechanisms of tropical Atlantic SST influence on North American hydroclimate variability. *J. Clim.* **23**, 5610–5628 (2010).
28. Ting, M., Kushnir, Y., Seager, R. & Li, C. Robust features of Atlantic multi-decadal variability and its climate impacts. *Geophys. Res. Lett.* **38**, <https://doi.org/10.1029/2011GL048712> (2011).
29. Deser, C. et al. Insights from Earth system model initial-condition large ensembles and future prospects. *Nat. Clim. Ch.* **10**, 277–286 (2020).
30. Eyring, V. et al. Overview of the coupled model intercomparison project phase 6 (CMIP6) experimental design and organization. *Geosci. Model Dev.* **9**, 1937–1958 (2016).
31. Henley, B. et al. Spatial and temporal agreement in climate model simulations of the Interdecadal Pacific Oscillation. *Env. Res. Lett.* **12**, 044011 (2017).
32. Capotondi, A., Deser, C., Phillips, A., Okumura, Y. & Larson, S. ENSO and pacific decadal variability in CESM2. *J. Adv. Mod. Earth. Syst.* **12**, e2019MS002022 (2020).
33. Power, S. et al. Decadal climate variability in the tropical Pacific: characteristics, causes, predictability, and prospects. *Science* **374**, eaay9165 (2021).
34. Coburn, J. & Pryor, S. C. Differential credibility of climate modes in CMIP6. *J. Clim.* **34**, 8145–8164 (2021).
35. Seager, R. et al. Strengthening tropical Pacific zonal sea surface temperature gradient consistent with rising greenhouse gases. *Nat. Clim. Ch.* **9**, 517–522 (2019).
36. Olonscheck, D., Rugenstein, M. & Marotzke, J. Broad consistency between observed and simulated trends on sea surface temperature patterns. *Geophys. Res. Lett.* **47**, e2019GL086773 (2020).
37. Watanabe, M., Dufresne, J., Kosaka, Y., Mauritsen, T. & Tatebe, H. Enhanced warming constrained by past trends in equatorial Pacific sea surface temperature gradient. *Nat. Clim. Ch.* **11**, 33–37 (2020).
38. Seager, R., Henderson, N. & Cane, M. A. Persistent discrepancies between observed and modeled trends in the tropical Pacific Ocean. *J. Clim.* **35**, 4571–4584 (2022).
39. Lee, S. et al. On the future zonal contrasts of equatorial pacific climate: perspectives from observations, simulation and theories. *NPJ Clim. Atmos. Sci.* **5**, 82 (2022).
40. Zhang, Y., Wallace, J. M. & Battisti, D. S. ENSO-like decade-to-century scale variability: 1900–93. *J. Climate* **10**, 1004–1020 (1997).
41. Deser, C., Phillips, A. S. & Hurrell, J. W. Pacific interdecadal climate variability: linkages between the tropics and the North Pacific during boreal winter since 1900. *J. Clim.* **17**, 3109–3124 (2004).
42. Trenberth, K. et al. Progress during TOGA in understanding and modeling global teleconnections associated with tropical sea surface temperature. *J. Geophys. Res.* **103**, 14291–14324 (1998).
43. Seager, R., Goddard, L., Nakamura, J., Naik, N. & Lee, D. Dynamical causes of the 2010/11 Texas-northern Mexico drought. *J. Hydromet.* **15**, 39–68 (2014).
44. Baek, S. et al. Precipitation, temperature, and teleconnection signals across the combined North American, Monsoon Asia, and Old World Drought Atlases. *J. Clim.* **30**, 7141–7155 (2017).
45. Madden, R. A. & Williams, J. The correlation between temperature and precipitation in the United States and Europe. *Mon. Wea. Rev.* **106**, 142–147 (1978).
46. Mueller, B. & Seneviratne, S. I. Hot days induced by precipitation deficits at the global scale. *Proc. Nat. Acad. Sci.* **109**, 12398–12403 (2012).
47. Schubert, S. D. et al. A U.S. CLIVAR project to assess and compare the responses of global climate models to drought-related SST forcing patterns: Overview and results. *J. Clim.* **22**, 5251–5272 (2009).
48. Schubert, S. D., Suarez, M. J., Piegion, P. J., Koster, R. D. & Bacmeister, J. T. Causes of long-term drought in the United States Great Plains. *J. Clim.* **17**, 485–503 (2004).
49. Hoerling, M. P. et al. Causes for the century-long decline in Colorado River flow. *J. Clim.* **32**, 8181–8203 (2019).
50. Cook, E. R. et al. Old World megadroughts and pluvials during the Common Era. *Sci. Adv.* **1**, e1500561 (2015).
51. Ault, T. R., Mankin, J., Cook, B. & Smerdon, J. Relative impacts of mitigation, temperature, and precipitation on 21st-century megadrought risk in the American Southwest. *Sci. Adv.* **2**, e1600873 (2016).
52. Chikamoto, Y., Timmermann, A., Widlansky, M. J., Balmaseda, M. & Stott, L. Multi-year predictability of climate, drought, and wildfire in southwestern north america. *Sci. Rep.* **7**, 6568 (2017).
53. Yeager, S. et al. Predicting near-term changes in the theee earth system: a large ensemble of initialized decadal predictions simulations using the Community Earth System Model. *Bull. Amer. Metoero. Soc.* **99**, 1867–1886 (2018).
54. Cai, W. et al. Pan-tropical climate interactions. *Science* **363**, eaav4236 (2019).
55. Heede, U. K., Federov, A. & Burls, N. A stronger versus weaker Walker: understanding model differences in fast and slow tropical Pacific responses to global warming. *Clim. Dyn.* **57**, 2505–2522 (2021).
56. Seager, R. et al. Model projections of an imminent transition to a more arid climate in southwestern North America. *Science* **316**, 1181–1184 (2007).
57. Chen, M., Xie, P. & Co-authors. CPC Unified Gauge-based Analysis of Global Daily Precipitation. In *Western Pacific Geophysics Meeting, Cairns, Australia, 29 July–1 August, 2008* (2008).
58. Hersbach, H. et al. The ERA5 global reanalysis. *Quart. J. Royal Meteor. Soc.* **146**, 1999–2049 (2020).
59. CAM team. CAM6 (Community Atmosphere Model 6), Model Item. OpenGMS. <https://geomodeling.njnu.edu.cn/modellItem/f36d9d3a-e937-46ac-ba7c-286886ccfad7> (2021).
60. Bogsenschutz, P. et al. The path to CAM6: coupled simulations with CAM5.4 and CAM5. *Geosci. Mod. Dev.* **11**, 235–255 (2018).
61. Hurrell, J. W., Hack, J. J., Shea, D., Caron, J. M. & Rosinski, J. A new sea surface temperature and sea ice boundary data set for the Community Atmosphere Model. *J. Clim.* **21**, 5145–5153 (2008).
62. Danabasoglu, G. et al. The community earth system model Version 2 (CESM2). *J. Adv. Mod. Earth Syst.* **12**, e2019MS001916 (2020).

63. Shin, S., Sardeshmukh, P. D., Newman, M., Penland, C. & Alexander, M. Impact of annual cycle on ENSO variability and predictability. *J. Clim.* **34**, 171–193 (2021).
64. Vimont, D., Newman, M., Battisti, D. S. & Shin, S. The role of seasonality and the ENSO mode in Central and East Pacific ENSO growth and evolution. *J. Clim.* **35**, 3195–3209 (2022).
65. Penland, C. & Sardeshmukh, P. The optimal growth of tropical sea surface temperature anomalies. *J. Clim.* **8**, 1999–2024 (1995).
66. von Storch, H., Burger, G., Schnur, R. & von Storch, J. Principal oscillation patterns: a review. *J. Clim.* **8**, 377–400 (1995).
67. Johnson, S., Battisti, D. & Sarachik, E. Seasonality in an empirically derived Markov model of tropical Pacific sea surface temperature anomalies. *J. Clim.* **13**, 3327–3335 (2000).
68. Rayner, N. et al. Global analyses of sea surface temperature, sea ice, and night marine air temperature since the late nineteenth century. *J. Geophys. Res.* **108**, 4407 (2003).
69. Penland, C. & Matrosova, L. Studies of El Niño and interdecadal variability in tropical sea surface temperatures using a non-normal filter. *J. Clim.* **19**, 5796–5815 (2006).
70. Frankignoul, C., Gastineau, G. & Kwon, Y. Estimation of the SST response to anthropogenic and external forcing and its impact on the Atlantic multidecadal oscillation and the Pacific Decadal Oscillation. *J. Clim.* **19**, 9871–9895 (2017).
71. Penland, C. & Matrosova, L. A balance condition for stochastic numerical models with application to the El Niño-Southern Oscillation. *J. Clim.* **7**, 1352–1372 (1994).
72. Newman, M., Shin, S. & Alexander, M. A. Natural variation in ENSO flavors. *Geophys. Res. Lett.* **38**, L14705 (2011).
73. Xu, T., Newman, M., Capotondi, A., Stevenson, S. & Alexander, M. An increase in marine heatwaves without significant changes in surface ocean temperature variability. *Nat. Com.* **13**, 7396 (2022).
74. Meinshausen, M. et al. The shared socio-economic pathway (SSP) greenhouse gas concentrations and their extensions to 2500. *Geosci. Model Dev.* **13**, 3571–3605 (2020).
75. Neelin, J. D., Langenbrunner, B., Meyerson, J. E., Hall, A. & Berg, N. California winter precipitation change under global warming in the coupled model intercomparison project Phase 5 ensemble. *J. Clim.* **26**, 6238–6256 (2013).
76. Allen, R. J. & Luptowitz, R. El Niño-like teleconnection increases California precipitation in response to warming. *Nat. Clim. Ch.* **8**, 16055 (2017).

## ACKNOWLEDGEMENTS

All authors were supported by NOAA award NA20OAR4310379. RS was additionally supported by NSF awards AGS-2127684 and AGS-2101214 and MT by NSF award AGS-1934358. We thank three anonymous reviewers and the editor for the useful comments and constructive criticisms.

## AUTHOR CONTRIBUTIONS

R.S. led the research team, conceived analyses and model experiments. M.T. conceived analyses and model experiments. P.A.A. performed the model simulations and conducted analyses and provided interpretation. J.N. performed analyses and contributed to interpretation. H.L. managed data, conducted analyses and contributed to interpretation. C.L. conducted analyses of SSTs and generated SST forcing data sets and contributed to interpretation. M.N. developed the linear inverse model for sea surface temperature. All authors edited and reviewed the manuscript.

## COMPETING INTERESTS

The authors declare no competing interests.

## ADDITIONAL INFORMATION

**Supplementary information** The online version contains supplementary material available at <https://doi.org/10.1038/s41612-023-00461-9>.

**Correspondence** and requests for materials should be addressed to Richard Seager.

**Reprints and permission information** is available at <http://www.nature.com/reprints>

**Publisher's note** Springer Nature remains neutral with regard to jurisdictional claims in published maps and institutional affiliations.



**Open Access** This article is licensed under a Creative Commons Attribution 4.0 International License, which permits use, sharing, adaptation, distribution and reproduction in any medium or format, as long as you give appropriate credit to the original author(s) and the source, provide a link to the Creative Commons license, and indicate if changes were made. The images or other third party material in this article are included in the article's Creative Commons license, unless indicated otherwise in a credit line to the material. If material is not included in the article's Creative Commons license and your intended use is not permitted by statutory regulation or exceeds the permitted use, you will need to obtain permission directly from the copyright holder. To view a copy of this license, visit <http://creativecommons.org/licenses/by/4.0/>.

© The Author(s) 2023